Acta Biomaterialia xxx (xxxx) xxx

Contents lists available at ScienceDirect

Acta Biomaterialia

journal homepage: www.elsevier.com/locate/actbio

Full length article

Genetically engineered bacterial magnetosomes as optimized tracers for magnetic particle imaging

Florian Thieben [a,b,c,1], Frank Mickoleit [e,1], René Uebe [e], Sophia Tessaro [e], Marina V. Dziuba [e], Javier Rández-Garbayo [d], Tim Magnus [d], Mandy Ahlborg [c], Justin Ackers [c], Peter Ludewig [d,*], Dirk Schüler [e,*], Tobias Knopp [a,b,c,**]

[a] Section for Biomedical Imaging, University Medical Center Hamburg-Eppendorf, Hamburg, Germany
[b] Institute for Biomedical Imaging, Hamburg University of Technology, Hamburg, Germany
[c] Fraunhofer IMTE, Fraunhofer Research Institution for Individualized Medical Technology and Engineering, Lübeck, Germany
[d] Department of Neurology, University Medical Center Hamburg-Eppendorf, Hamburg, Germany
[e] Department of Microbiology, University of Bayreuth, Bayreuth, Germany

ARTICLE INFO

Keywords:
Magnetic Particle Imaging
Tracer
Iron oxide nanoparticles
Magnetosomes
Genetic engineering

ABSTRACT

Medical imaging relies on tracer materials to enable accurate visualization and diagnosis of diseases. Magnetic Particle Imaging (MPI) is an innovative tomographic modality that offers exceptional sensitivity and temporal resolution. These characteristics make MPI particularly promising for clinical applications such as real-time vascular and perfusion imaging, tumor detection, and intraoperative guidance. However, MPI performance has so far been limited by the quality of available tracers, as conventional chemical synthesis provides only restricted control over the size, shape, and magnetic properties of iron oxide nanoparticles. Biogenic magnetic nanoparticles, so-called magnetosomes, produced by magnetotactic bacteria, represent a compelling alternative. Magnetosome biosynthesis is fully genetically encoded, enabling the natural formation of magnetite nanoparticles with uniform size and morphology, which is difficult to achieve through chemical synthesis. Moreover, genetic engineering of the bacterial production host allows precise tuning of particle characteristics, including size, shape, and magnetic behavior, to meet specific application requirements. In this study, magnetosomes isolated from different *Magnetospirillum gryphiswaldense* mutant strains, each biomineralizing particles with distinct core diameters, were systematically evaluated as potential MPI tracers. Magnetic particle spectroscopy (MPS) was used to identify the most promising candidates based on their signal properties. These tracers were subsequently subjected to detailed signal analyses and phantom experiments to directly compare their imaging performance. Our findings demonstrate that genetically tailored magnetosomes can substantially improve MPI signal quality, underscoring their potential as next-generation tracers. This work provides a foundation for the rational design of optimized biogenic nanoparticles to advance preclinical and future clinical MPI applications.
Statement of significance: Magnetic Particle Imaging (MPI) is a novel imaging technology with high sensitivity and real-time capabilities, making it highly promising for clinical applications such as blood flow monitoring and tumor detection. The performance of MPI strongly depends on the properties of the tracer materials used. However, producing high-quality tracers through conventional chemical synthesis remains challenging. In this study, we introduce an innovative biological approach by using genetically engineered magnetotactic bacteria to produce uniform magnetic nanoparticles, so-called magnetosomes. This strategy allows precise control of particle size, shape, and magnetic properties, resulting in tracers with superior performance. Our findings pave the way for the development of next-generation MPI tracers, advancing both fundamental research and potential clinical translation.

* Corresponding authors.
** Corresponding author at: Section for Biomedical Imaging, University Medical Center Hamburg-Eppendorf, Hamburg, Germany.
E-mail addresses: p.ludewig@uke.de (P. Ludewig), dirk.schueler@uni-bayreuth.de (D. Schüler), t.knopp@uke.de, tobias.knopp@tuhh.de (T. Knopp).
[1] These authors contributed equally to this work.

https://doi.org/10.1016/j.actbio.2026.05.048
Received 4 November 2025; Accepted 28 May 2026
Available online 29 May 2026

1. Introduction

Medical imaging is an indispensable tool in modern medicine, enabling early diagnosis, treatment monitoring, and a deeper understanding of physiological and pathological processes. Among emerging modalities, Magnetic Particle Imaging (MPI) has gained attention as a novel tomographic technique that directly visualizes magnetic nanoparticle tracers without background signal. First introduced by *Gleich and Weizenecker* [1], MPI is free of ionizing radiation and provides quantitative, three-dimensional images with exceptional temporal resolution (up to 21.5 ms) and tracer sensitivity in the picogram iron range (896 pg $_{Fe}$) [2]. These characteristics make MPI particularly promising for dynamic real-time applications, such as vascular and perfusion imaging, tumor detection, and intraoperative guidance.

In contrast to anatomical imaging techniques, MPI depicts only the tracer distribution, resulting in very high signal-to-noise ratios (SNR). Signal generation relies on the non-linear magnetization response of tracers to applied magnetic fields. A selection field creates a field-free point (FFP) or field-free line (FFL), where an oscillating drive field excites only tracers within this low-field region, while particles outside remain saturated. Moving this field-free region across the field of view (FOV) enables spatial encoding, and the resulting signal is linear and quantitative with respect to tracer concentration [3]. Beyond imaging, MPI can also manipulate particles using magnetic forces and extract functional information such as temperature or viscosity, enabling multi-contrast imaging with a broad spectrum of future applications [4–6]. Over the past decade, preclinical studies have highlighted the strong potential of MPI for clinical translation, with proof-of-concept experiments demonstrating its value in vascular diagnostics, targeted therapy, and the real-time detection of acute conditions such as ischemic stroke and gastrointestinal bleeding [7–10].

Recent advances in hardware are paving the way toward human-sized MPI scanners [11–13]. However, the full potential of MPI critically depends on the availability of optimized, clinically approved tracers [14]. Currently, most MPI tracers are synthetic iron oxide nanoparticles (*magnetic nanoparticles*, MNPs) composed of magnetite (Fe_3O_4) or maghemite (γ-Fe_2O_3) cores, typically 10–100 nm in size. These particles are attractive due to their straightforward synthesis, stability, and favorable biocompatibility [15,16]. Yet, reproducibility and precise control over size, shape, and magnetic properties remain challenging [17,18]. Moreover, surface modifications are often required to stabilize particles for biomedical use [19]. For high-quality MPI performance, tracers must exhibit superparamagnetism, short magnetic relaxation times, low anisotropy, and uniform core size and shape [20–22]. These requirements are particularly critical for human imaging, where low drive-field amplitudes are necessary to prevent peripheral nerve stimulation [23,24].

Magnetosomes, biologically synthesized MNPs produced by magnetotactic bacteria, represent a promising alternative to synthetic tracers. In the model organism *Magnetospirillum gryphiswaldense*, magnetosomes consist of highly uniform, cuboctahedral magnetite crystals enclosed by a phospholipid membrane (magnetosome membrane, ~5 nm in thickness) containing specific proteins essential for biomineralization [25–27]. These intracellular vesicles act as natural nanoreactors [28,29], enabling strict control of crystal growth and yielding nanoparticles with exceptional homogeneity, high crystallinity, and narrow Gaussian to log-normal size distributions that can hardly be achieved by chemical synthesis [30–32]. The magnetite core consists mainly of a (single) magnetic domain, and saturation magnetization values of up to 410 kA/m [33] and 90–110 emu/g Fe [34] have been reported. The surrounding magnetosome membrane leads to a negative particle surface charge, as indicated by zeta potential values of −34 to −38 mV [35–38]. Recently, the colloidal stability / aggregation behavior of magnetosomes was systematically assessed when incubated in different buffer solutions and cell culture media [39]. Although with prolonged incubation time (up to 48 h) a tendency for the formations of magnetosome chains and smaller aggregates was observed, the particles showed colloidal stability under a variety of conditions – a prerequisite for future *in vivo* applications.

Since the late 1980s, magnetosomes have been suggested as ideal agents for magnetic imaging due to their inherent material properties [40–42]. A unique advantage of magnetosomes is that their biosynthesis is entirely genetically encoded by over 30 genes, allowing precise genetic engineering to tailor their magnetic properties. Deletion or overexpression of specific genes can shift particle size and magnetic behavior, generating variants ranging from unstable superparamagnetic to stable ferrimagnetic states [29,31,32,43]. Initial studies demonstrated that magnetosomes with core sizes around 30 nm exhibit optimal MPI performance [33,44,45], consistent with theoretical predictions for drive fields at ~26 kHz [46].

Building on these findings, this study systematically investigates genetically engineered magnetosome variants with tailored core sizes. Using magnetic particle spectroscopy (MPS) and phantom MPI experiments, we evaluate their signal responses and imaging performance, aiming to establish magnetosomes as next-generation tracers that could significantly enhance MPI and broaden its applications in biomedical imaging.

2. Materials and methods

2.1. Bacterial strains and cultivation conditions

For the production of size-adjusted magnetosome samples, genetically modified *M. gryphiswaldense* strains lacking various genes important for crystal growth (Δ*mamR* [29]), magnetosome membrane assembly (Δ*mamF*, Δ*mmsF*/Δ*mamF*) (each from [29]), magnetosome chain arrangement (Δ*mamJ* [47]), or encoding cellular iron transporters (Δ*feoAB1* [44], Δ*feoAB12* double mutant [45], Δ*Fe4* iron uptake mutant [31]) were used. Loss of these genes results in a stepwise reduction in magnetite crystal size due to crystal growth defects or reduced cellular iron uptake, or the formation of magnetosome clusters instead of regular chains [26,27] (Table S1).

The respective strains (wildtype/WT and mutants) were grown in modified flask standard medium (FSM; 10 mM 4-(2-hydroxyethyl)-1-piperazineethanesulfonic acid (HEPES), 15 mM potassium lactate, 4 mM $NaNO_3$, 0.74 mM KH_2PO_4, 0.6 mM $MgSO_4$, 50 μM Fe(III)-citrate, 3 g L^{-1} soy peptone, 0.1 g L^{-1} yeast extract, pH 7.0) as previously described [48]. Cultivation was performed in 5 L flasks under moderate shaking (120 rpm) at 28°C, applying a headspace-to-liquid ratio of ~1:4 with air in the headspace. Under these conditions, the oxygen concentration in the medium declined with increasing cell density, thereby reaching microoxic conditions and inducing magnetosome biosynthesis [49,50]. Cells were harvested in the late exponential growth phase by centrifugation (9000 x *g*, 20 min, 4°C). Afterwards, cell pellets were resuspended in 20 mM HEPES, 5 mM ethylenediaminetetraacetate (EDTA), pH 7.2, and stored at −20°C until further use.

2.2. Magnetosome isolation

For the isolation of intact magnetosomes, a two-step purification procedure was applied consisting of a magnetic separation and a sucrose high-density ultracentrifugation step [51,52]. Cell pellets of microoxically grown *M. gryphiswaldense* cultures (WT or mutant strains) were resuspended in 20 mM HEPES, 5 mM EDTA (pH 7.2), and disrupted by 3–5 passages through a microfluidizer system (M-110 L, Microfluidics Corp., Westwood, MA, USA) equipped with a H10Z interaction chamber at 124 MPa. The crude extracts were passed through a MACS magnetic-separation column (5 mL; Miltenyi, Bergisch Gladbach, Germany) placed between two neodymium-iron-boron magnets (each 4.0 cm x 2.0 cm x 1.0 cm, 1.3 T). Thereby, non-magnetic cellular compounds passed the column and were instantly eluted whereas the magnetosomes were retained within the column. In order to remove impurities, the

column was washed with 50 mL extraction buffer (10 mM HEPES, 1 mM EDTA, pH 7.2), followed by 50 mL high-salt buffer (10 mM HEPES, 1 mM EDTA, 150 mM NaCl, pH 7.2), and again 50 mL extraction buffer. Afterwards, the magnets were removed, and the magnetosomes were eluted with double-distilled water (ddH_2O). The magnetosome suspension was then centrifuged through a 60% (w/v) sucrose cushion (in 10 mM HEPES, 1 mM EDTA, pH 7.2) for 2 h at 200,000 x *g* and 4°C. Because of their high density, the magnetosomes pelleted at the bottom of the tube, whereas residual cellular constituents were retained by the sucrose cushion. Finally, the particles were resuspended in ddH_2O and stored in Hungate tubes at 4°C under a nitrogen atmosphere until further use.

With focus on future *in vivo* experiments, magnetosome suspensions were sterile-filtrated prior to analyses as previously described [53]. Briefly, the suspensions were diluted with ddH_2O to a final concentration of ~50 μg Fe mL^{-1}, and sterile-filtrated using a 0.22 μm PVDF sterile-filter (Roth, Karlsruhe, Germany). After filtration, the suspensions were concentrated again to obtain final Fe concentrations of 2 mg mL^{-1}. Using this protocol, for statistical analysis multiple charges of each magnetosome type were produced.

2.3. Transmission electron microscopy (TEM)

For TEM analyses of whole cells or isolated magnetosomes, the respective samples (concentrated cell suspensions or highly diluted magnetosome suspensions) were directly deposited onto carbon-coated copper grids (Science Services, Munich, Germany). Magnetosome samples were additionally stained with 2% uranyl acetate. TEM was performed on a JEM-1400Plus transmission electron microscope (JEOL, Tokyo, Japan) operated with an acceleration voltage of 80 kV. Magnetosome sizes were measured from TEM micrographs using the software ImageJ version 1.44p [54].

2.4. Determination of iron concentrations

Suspensions of magnetosomes isolated from the WT and mutant strains were normalized to their overall iron concentration. The iron content (mg Fe mL^{-1}) was determined by atomic absorption spectroscopy (AAS). Sample volumes of 5–20 μL were mixed with 69% nitric acid (final volume 1 mL) and incubated for 3 h at 98°C. Afterwards, the samples were diluted with ddH_2O to receive a final volume of 3 mL. Iron measurements were performed using a contrAA300 high-resolution atomic absorption spectrometer (Analytik Jena, Jena, Germany) equipped with a 300 W xenon short-arc lamp (XBO 301, GLE, Berlin, Germany) as continuum radiation source. The equipment presented a compact high-resolution double monochromator (consisting of a prism pre-monochromator and an echelle grating monochromator) and a charge-coupled device (CCD) array detector with a resolution of about 2 pm per pixel in the far ultraviolet range. An oxidizing air/acetylene flame was used to analyze the samples (wavelength 248.3 nm). The number of pixels of the array detector used for detection was 3 (central pixel 1). Measurements were performed in quintuplicates, each as a mean of three technical replicates ($n = 15$).

2.5. Dynamic light scattering (DLS) measurements

Zeta potential values and magnetosome hydrodynamic diameters were determined by DLS analysis using a Zetasizer Nano-ZS (Malvern Panalytical, Malvern, UK) at a wavelength of 638 nm in automatic mode at 25°C. Measurements were performed on diluted magnetosome suspensions (0.10 mg Fe mL^{-1}) isolated from the WT of *M. gryphiswaldense* or mutant strains as indicated; *perimag* nanoparticles (micromod Partikeltechnologie GmbH, Germany) at the same iron concentration served as a control. Each sample was analyzed in quintuplicates on three technical replicates ($n_{total} = 15$) using DTS1070 cuvettes (Malvern Panalytical, Malvern, UK). The evaluation software provided by the supplier (Malvern Panalytical Zetasizer Software 7.13) is based on the Cumulant method and uses the Stokes-Einstein Equation for size determination. Intensity- and volume-weighted particle size distributions were used to compare particle sizes from different magnetosome types.

2.6. Nanoparticle sedimentation assay

The sedimentation behavior of purified nanoparticles (*i.e.*, their tendency to settle in suspension as a measure of colloidal stability) was analyzed as described previously [36,38]. In brief, the optical density of a particle suspension (0.10 mg Fe mL^{-1}) was monitored over time at a wavelength of 508 nm (Evolution 201 UV–Visible Spectrophotometer; Thermo Fisher Scientific, Waltham, MA, USA). Absorption values were normalized to the initial reading at t = 0 h (start of the experiment), thereby enabling direct comparison across different particle suspensions. All measurements were performed at least in triplicate ($n \geq 3$).

2.7. Tailored magnetic particle imaging nanoparticles – perimag

The aim was to compare the magnetosome samples with the commercially available MPI gold standard tracer, *perimag* (micromod Partikeltechnologie GmbH, Germany). It is composed of nanoparticle clusters enveloped by a dextran shell, with a reported hydrodynamic diameter of 130 nm, a magnetic core diameter of about 19 nm, and iron core sizes (individual particles) ranging from 3 nm to 8 nm [55,56].

2.8. Magnetic particle spectroscopy parameters

In contrast to Magnetic Particle Imaging (MPI), magnetic particle spectroscopy (MPS) enables the direct assessment of magnetic nanoparticle dynamics without the need for image reconstruction. The measured signal amplitude and its relaxation behavior in the time-domain, together with the harmonic decay observed in the frequency-domain, provide quantitative information on the dynamic response of the tracer material under oscillatory excitation fields. These parameters permit an evaluation of the suitability of specific tracers for multi-dimensional drive-field excitation in MPI. By applying additional offset fields, the static point spread function (PSF) can be determined experimentally. From this PSF, the full width at half maximum (FWHM) in the x-space representation can be calculated, which serves as a quantitative parameter for spatial resolution in MPI.

Dynamic MPS measurements were performed using a calibrated custom-built MPS system operating at a drive-field frequency of $f =$ 26.042 kHz. For each measurement, 1000 periods were averaged, and the sampling rate was set to 7.8125 MS/s [57]. Static PSF measurements were conducted on a second calibrated custom-built MPS system specifically designed for offset-field experiments and equipped with additional offset-field coils [58]. In this system, the drive-field frequency was $f = 25.0$ kHz and the sampling rate was 15.625 MS/s, with 500 periods averaged for each offset-field value.

In the initial experiment, the time-domain signal was determined at a drive-field amplitude of 20 mT/μ_0. For each magnetosome type and three independent batches ($n = 3$), a sample volume of 10 μL with an iron concentration of 2 mg Fe mL^{-1} (35.7 mmol L^{-1}) was used. To evaluate tracer performance with respect to MPI, particularly for multi-dimensional excitation, a detailed analysis was conducted on one representative batch. The positive half-wave of the dynamic PSF in the time-domain was examined to highlight relaxation effects. In the frequency-domain, the odd harmonics of the magnetic moment were analyzed to characterize harmonic decay. To enhance comparability between tracers, harmonic amplitudes were additionally normalized to a reference measurement obtained with *perimag*.

Magnetic relaxation was quantified directly from the time-domain MPS signal using a model-free cross-correlation approach. The measured waveform was separated into positive and negative drive-field scan directions. In the adiabatic, quasi-static regime of magnetic particle imaging, both half-cycles are expected to exhibit mirror symmetry,

reflecting an instantaneous alignment of the magnetic moments with the applied field. Deviations from this symmetry indicate non-adiabatic behavior arising from finite Néel and Brownian relaxation processes [59]. The mirrored negative half-cycle was cross-correlated with the positive half-cycle, and the lag corresponding to the maximum of the cross-correlation function was determined. While alternative methods, such as TAURUS [60], exist for quantifying relaxation, we opted for the model-free cross-correlation approach because it provided stable and straightforward estimation of the effective relaxation time under our experimental conditions. Since the relative displacement between the two scan directions corresponds to twice the underlying physical delay, the effective relaxation time was defined as

$$\tau_{\mathrm{eff}} = \frac{\mathrm{k}^*}{2}\Delta \mathrm{t},$$

where k* denotes the lag at maximum correlation and Δt represents the sampling interval.

For the most promising tracer candidate, MPS hysteresis curves were recorded at four drive-field amplitudes H ∈ {6, 10, 14, 20} mT/μ_0. In addition, a dilution series covering iron concentrations from 1.1 to 35.7 mmol L^{-1} was prepared to investigate signal linearity, which was assessed using the third harmonic amplitude. FWHM experiments were performed at the same set of drive-field amplitudes using *perimag* and Δ*feoAB1* samples with an iron concentration of 2 mg Fe mL^{-1} (35.7 mmol L^{-1}) and a sample volume of 100 μL. Offset fields were varied in 0.2 mT increments over a range from −25 mT to 25 mT to determine the static PSF and the corresponding FWHM.

2.9. Bruker MPI scanner parameters

MPI, in contrast to MPS, measures the nonlinear magnetization of spatially distributed tracer material. Utilizing reconstruction methods, the spatial distribution is imaged. All MPI measurements performed in this work were carried out with a preclinical Bruker MPI system 25/20 FF (Bruker Biospin MRI GmbH, Germany). The scanner topology is an FFP setup, with a maximal gradient strength G_z up to 2.5 T/m in the z-direction and −1.25 T/m in x- and y-directions. The drive-field amplitude can be set to a maximum of 14 mT/μ_0 in x-, y- and z-directions. The excitation frequencies are given by $f_x = 2.5/102$ MHz, $f_y = 2.5/96$ MHz and $f_z = 2.5/99$ MHz. Generally, an MPI system must be recalibrated once a system parameter changes, including the use of different tracer types. The system matrix measurement technique is a calibration process in MPI, it is mainly used for image reconstruction and is acquired as the particle signal response from each location within a defined FOV [61]. Further, a quantitative comparison of different tracers on system matrix level can be done by considering the signal-to-noise ratio (SNR) profiles [62].

2D system matrices were measured on a FOV size of 21 mm x 21 mm in x- and y-direction. For each tracer, a delta-sample with 2 × 2 × 1 mm^3 or 4 μL and a concentration of 35.7 mM iron was used. The drive-field amplitude was set to 12 mT/μ_0 and the maximum gradient was set to 2 T/m. The delta-sample was placed by a robot on 21 × 21 grid positions and measured with 100 averages per grid position. The quality of the system matrices was assessed using the SNR values of the x-receive channel [62]. For a set of frequencies kf_0, based on mixing factors k_x and k_y with $k(k_x, k_x) = (k_x + 1)\ 16 + (k_y + 1)\ 17$ and $f_0 = 1531.86$ Hz, dedicated system matrix pattern are selected for comparison.

Image reconstruction was performed with two line-phantoms, one with 12 × 1 × 4 mm^3 and one with 10 × 1 × 4 mm^3 containing 35.7 mM iron. The phantoms were orientated once in x- and once in y-direction with a 5 mm edge-to-edge distance. Additionally, for the best-performing candidate and *perimag*, a v-phantom consisting of a hollow cylinder with 0.9 mm diameter and an angular opening of 60° was filled with 14 μL tracer (35.7 mM).

Utilizing the reconstruction framework MPIReco.jl [63], single-frame reconstructions were performed on an interpolated grid of 51 × 51 pixels to simulate low SNR conditions. For quantitative evaluation, all 1000 acquired frames were reconstructed individually (n = 1000), and the normalized root-mean-square error (NRMSE) and structural similarity index measure (SSIM) were calculated relative to a voxelized ground truth generated from the CAD files [64].

To bridge the gap toward biological relevance without conducting *in vivo* experiments, a scaled rat phantom was implemented based on the anatomical model described by *Exner et al.* [65]. The phantom geometry was uniformly scaled to 70% of its original size in all spatial dimensions, resulting in a volume reduction by a factor of 2.92. Consequently, the original organ volumes were reduced to 4821 mm^3 for the liver and 540 mm^3 for the brain, while the tracer concentrations were maintained. Organ-specific tracer concentrations were assigned according to the reported steady-state *in vivo* values, with tracer exclusively distributed in the liver (270 μg Fe mL^{-1}, 4.83 mmol L^{-1}) and brain (74 μg Fe mL^{-1}, 1.33 mmol L^{-1}) compartments to emulate physiological accumulation. Image reconstruction was performed using a system matrix acquired on a regular grid of 40 × 40 × 20 positions covering a FOV of 50 mm x 50 mm x 30 mm. The system matrix acquisition and phantom measurements were conducted with drive-field amplitudes of 12 mT/μ_0 and a maximum gradient strength of 1.2 T/m. For both acquisitions, 46 averages were applied to ensure consistent SNR conditions.

2.10. Statistical methods

If not otherwise stated, data were reported as mean ± standard deviation (SD), and n represents the number of independent experiments (technical or biological replicates). The size of magnetite crystals in magnetosome samples was measured from TEM micrographs using ImageJ [54] and data was plotted with the Fit-o-mat software [66]. Standard deviations were calculated using the Statistics standard library of the Julia programming language (JuliaLang) and SigmaPlot 12.0 software (Systat Software Inc., San Jose, CA, USA), which was also used for statistical analysis.

Significance of differences in magnetosome crystal size was assessed using a Kruskal-Wallis test followed by Dunn's post hoc test with Bonferroni correction. Data from replicate experiments were pooled prior to statistical analysis. Zeta potential group comparisons, MPS signal amplitude measurements, and MPI reconstruction comparison were conducted using Welch's t-test (two-tailed) assuming unequal variances. Statistical significance was defined at $p < 0.05$. Pearson correlation analysis was used to demonstrate the linear relationship between TEM and DLS particle size measurements. Linear regression analysis was performed on MPS dilution series measurements to assess the relationship between iron concentration and MPS signal.

For image processing, GIMP software (GNU Image Manipulation Program, version 2.10.38) and Adobe Illustrator CS6 (Adobe Systems Inc., San Jose, CA, USA) were used.

3. Results

3.1. Structural characterization

Magnetosomes were purified from the unmodified WT of *M. gryphiswaldense* and mutant strains Δ*mamJ*, Δ*mamR*, Δ*mamF*, Δ*mmsF/*Δ*mamF*, Δ*feoAB1*, Δ*feoAB12*, and Δ*Fe4*, in which different biosynthetic magnetosome genes or iron uptake systems were deleted (Table S1). TEM images of magnetosomes isolated from the respective strains (Figs. 1 and S2) revealed homogeneous particle suspensions with a mostly uniform geometry and only minimal deviations from the cuboctahedral shape of WT particles (Fig. 2). Depending on the strain, magnetosomes with average core sizes ranging from 21 to 40 nm were produced. Magnetosome samples with smaller core diameters exhibited a weak tendency towards lower standard deviations and thus, a narrower size distribution. Δ*feoAB1*, Δ*feoAB12*, Δ*Fe4* and Δ*mmsF/*Δ*mamF*

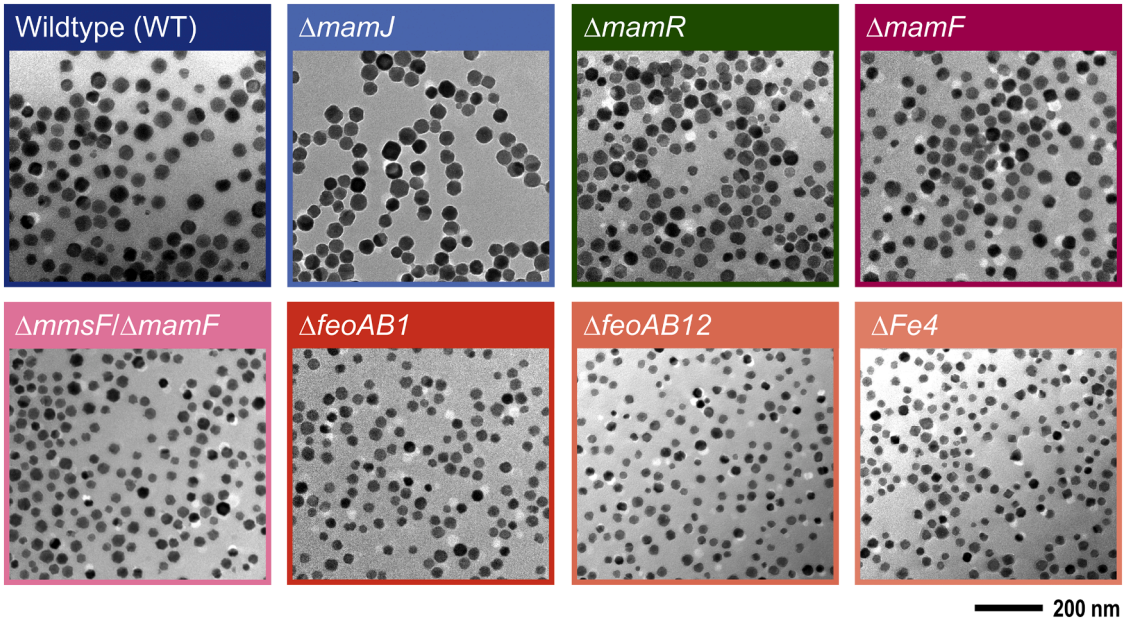

Fig. 1. Transmission electron microscopy (TEM) micrographs of suspensions of different magnetosome types. Particles were isolated from the respective strains according to published procedures [51,52] and in addition, sterile-filtrated to remove bacterial contaminations [53]. The resulting suspensions were free of impurities and contained well-dispersed particles.

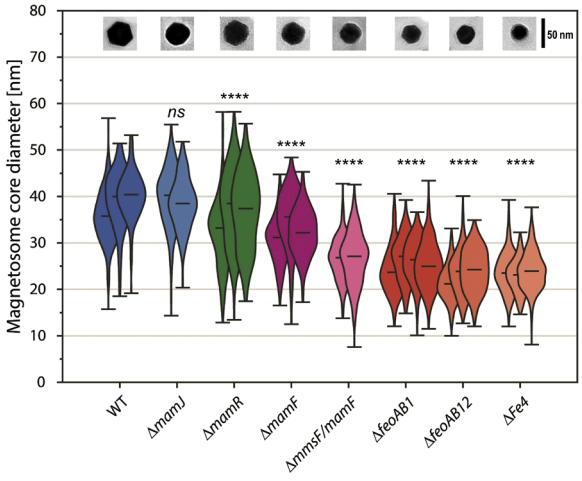

Fig. 2. Magnetosome core size distribution. Violin plot of the core sizes of magnetosomes isolated from different *M. gryphiswaldense* strains as indicated. Each particle suspension was analyzed by TEM, and ImageJ software was used to determine the mean core diameters ($n \geq 350$). The insets show TEM micrographs of a representative magnetosome particle isolated from the respective strain. Differences in particle size distributions relative to the WT were assessed using a Kruskal-Wallis test followed by Dunn's post hoc test with Bonferroni correction. Significance levels indicated in the figure correspond to ****, $p < 0.0001$; *ns*, not significant.

showed a significantly reduced particle size compared to the WT, with the smallest mean core diameter of 21.4 nm being measured for Δ*feoAB12* (Table S2). The respective particle sizes measured from TEM images agreed well with the superparamagnetic domain size range between 21 and 28 nm. However, for Δ*mamR*, Δ*mamJ*, and Δ*mamF* mutant strains larger-sized magnetosomes of 30 to 36 nm were produced being within the ferrimagnetic size range.

Although magnetosome purification narrows the particles' size distribution [52], particles from all strains were still polydisperse to some extent, which can be attributed to the presence of immature magnetosomes. Magnetosomes of the ferrimagnetic size range resembled matured, unmodified WT particles, with the typical cuboctahedral structure (Figs. 1, S2). Nevertheless, it is difficult to determine the 3 dimensions lattice of each crystal without thickness measurements. Magnetosomes with a core diameter larger than 30 nm are probably magnetically blocked at room temperature and thus tend to form chains, rings or aggregates due to magnetic interactions as described previously (Figs. 1, S2) [67,68].

In dynamic light scattering (DLS) analyses on diluted magnetosome suspensions (0.1 mg Fe mL^{-1}), increased particle diameters were measured (compared to TEM) as DLS additionally accounts for the contribution of the hydration shell that surrounds the particles (hydrodynamic diameter, Table 1). However, the relative ordering and size hierarchy of the different particle types was preserved. Accordingly, a

Table 1
Effective relaxation times τ_{eff}, determined from cross-correlation of the positive and negative half-waves of the dynamic time-domain signal response, and the corresponding particle sizes (*i.e.* core sizes measured by TEM and hydrodynamic diameters obtained from DLS analyses).

Particle type	τ_{eff} / µs	Core size (TEM) / nm	Hydrodynamic diameter (DLS) / nm	
			Intensity-weighted*	Volume-weighted**
perimag	1.41	3.3***	133.4 ± 52.1	79.5 ± 16.1
Δ*feoAB1*	1.80	24.1	76.8 ± 26.6	57.4 ± 20.7
Δ*feoAB12*	1.41	21.4	74.9 ± 23.8	58.9 ± 19.0
Δ*Fe4*	1.93	23.7	75.5 ± 32.7	52.8 ± 22.0
Δ*mamJ*	2.70	39.8	120.7 ± 40.6	81.8 ± 29.3
Δ*mamR*	2.95	32.6	126.8 ± 85.9	111.6 ± 61.8
Δ*mamF*	4.24	30.8	100.1 ± 31.0	77.8 ± 31.8
Δ*mmsF* / Δ*mamF*	1.67	26.7	90.8 ± 35.8	65.2 ± 28.4
wildtype WT	2.18	35.9	134.6 ± 39.5	83.2 ± 24.9

* reflects the measured scattering signal thereby favoring larger particle diameters due to the strong size dependence of the scattering intensity (Rayleigh approximation, $I \propto d^6$);
** reflects the distribution of total particle volume across different size classes and thus, provides a more representative estimate of the actual size distribution;
*** core diameter of individual *perimag* particles, forming clusters with a magnetic diameter of 19 nm [55].

strong and statistically significant, positive linear correlation between TEM and DLS particle sizes was obtained (Pearson's $r = 0.93$, $p < 0.01$, $n = 7$), indicating consistent scaling between core and hydrodynamic particle diameters. Δ*mamR* magnetosomes showing a markedly higher DLS value compared to the overall trend (111.6 ± 61.8 nm, volume-weighted; Table 1) were excluded from the correlation analysis due to the presence of different particle size classes (as obvious from TEM micrographs, Figs. 1, 2) and its pronounced polydispersity.

3.2. Magnetic particle spectroscopy (MPS) analysis

MPS was used to evaluate the magnetic performance of each magnetosome type and to benchmark them against the commercial MPI tracer *perimag* (micromod Partikeltechnologie, Rostock, Germany) using our custom MPS system [57]. Measurements were performed on 10 µL samples containing 2 mg Fe mL^{-1} at a drive-field amplitude of 20 mT/μ_0 and frequency of 26.042 kHz (Fig. 3). Samples of the MPI tracer *perimag* at the same volume and iron concentration were included as a reference. The resulting tracers were classified as either high-performing or suboptimal based on their signal characteristics.

For better visualization in time-domain, only the positive half-wave of the MPS signal response is shown in form of the dynamic point spread function (PSF). In the time-domain, high-performing magnetosome types (Δ*feoAB1,* Δ*feoAB12,* Δ*Fe4*) exhibited a MPS signal response with a single, symmetric amplitude, and relaxation behavior similar to *perimag*. Suboptimal variants (Δ*mamR*, Δ*mamJ,* Δ*mamF,* Δ*mmsF*/Δ*mamF*) with an increased particle size (Table S2) displayed a strong relaxation behavior, and the loop started to open up, indicating the onset of coercivity with increasing particle size. Moreover, the MPS signal responses provided a delayed maximum or more than one local maximum, displaying a suboptimal signal response. Among all tested variants, Δ*feoAB1* showed the strongest response, with a 2.98-fold higher amplitude compared to *perimag* ($p = 0.043$, $n = 3$; Welch's *t*-test).

In the frequency domain, the odd harmonics of the MPS signal response are shown for Δ*feoAB1*, Δ*feoAB12*, and Δ*Fe4* as high-performing tracers. High-performing candidates demonstrated a strong signal with slower harmonic decay, which is advantageous for the reconstruction process, a key parameter for spatial resolution in MPI. In contrast, magnetosome samples isolated from Δ*mamR*, Δ*mamJ*, Δ*mmsF*/Δ*mamF*, and Δ*mamF* strains did not show the desired signal response, which can be identified in a non-smooth harmonic decay.

For direct comparison, the odd harmonics normalized to the reference signal response of *perimag* are shown (Fig. 3). High-performing tracer candidates showed a smooth amplified signal response. Δ*feoAB1* yielded the highest relative signal strength. Below 1 MHz, an oscillation of the normalized signal response of Δ*mamR*, Δ*mmsF*/Δ*mamF* and Δ*mamF* was visible. Δ*Fe4* and Δ*mamJ* provided a stronger signal only for frequencies below 500 kHz.

Table 1 presents the effective relaxation times alongside the corresponding magnetic core diameters for all investigated particle types. The measured relaxation times range from 1.41 µs to 4.24 µs, with core diameters of individual particles spanning 3.3 nm for *perimag* to 39.8 nm for Δ*mamJ*, reflecting a broad dynamic range among the samples (it should be noted that *perimag* consists of particle clusters with an overall magnetic diameter of 19 nm [55]). A moderate positive correlation between core size and relaxation time is observed, indicating that larger cores exhibit slower magnetization dynamics, although the relationship is not strictly monotonic.

In Fig. 4, the correlation between the mean core size and the maximum MPS signal intensity is presented for three biological replicates. When excited with a 20 mT/μ_0 drive-field amplitude, the mutant strains Δ*feoAB1*, Δ*feoAB12*, and Δ*Fe4* exhibited the highest signal amplitudes, which correlated with a mean crystal size below 28 nm. Most mutant magnetosome samples exceeded the signal amplitude of the reference tracer *perimag*, with Δ*mamF* showing the strongest response. However, the apparent superiority of magnetosomes with larger core sizes was limited to one-dimensional excitation under high drive-field amplitudes, as the evaluation of the signal response shown in Fig. 3 revealed suboptimal behavior under these conditions. In contrast, WT magnetosomes with a larger mean core diameter of approximately 35–40 nm generated the lowest signal among all investigated samples.

A more detailed MPS characterization of the best-performing

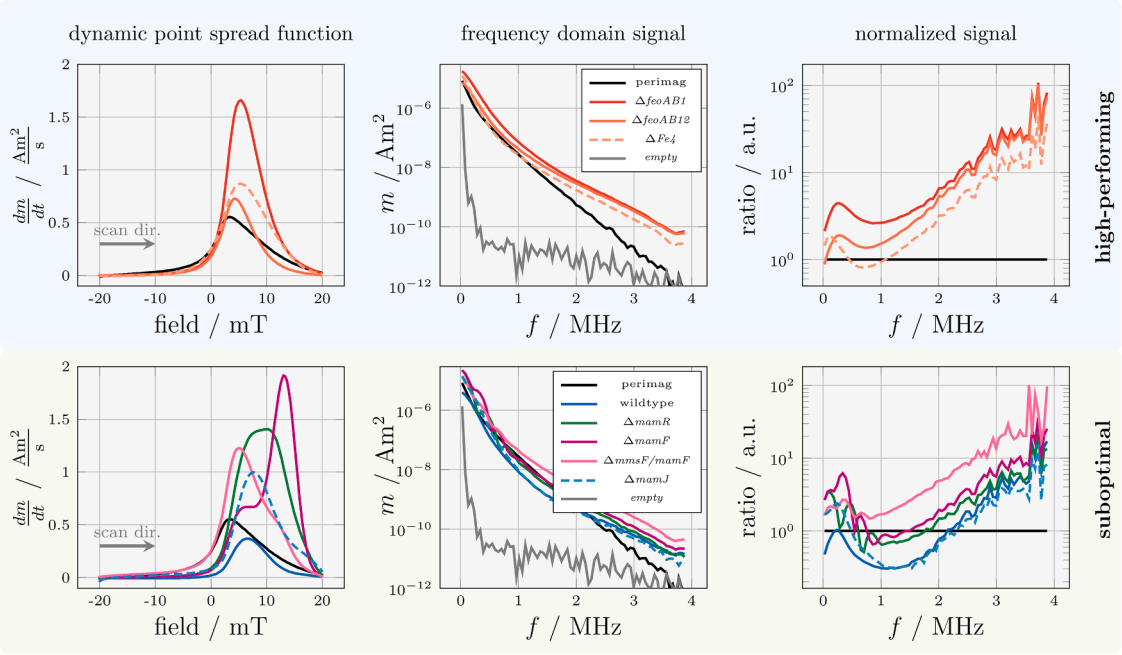

Fig. 3. MPS signal response in time domain and frequency domain. The different magnetosome types investigated are categorized into high-performing tracers for MPI (Δ*feoAB1,* Δ*feoAB12,* Δ*Fe4*) and suboptimal candidates (Δ*mamR*, Δ*mamJ*, Δ*mamF*, Δ*mmsF*/Δ*mamF*, and WT). In time domain, the positive half-wave of the dynamic point spread function is shown for a single replicate of each type, with *perimag* serving as reference. In frequency domain, the odd harmonics of the magnetic moment are shown together with an empty measurement. Additionally, the odd harmonics normalized to *perimag* are provided.

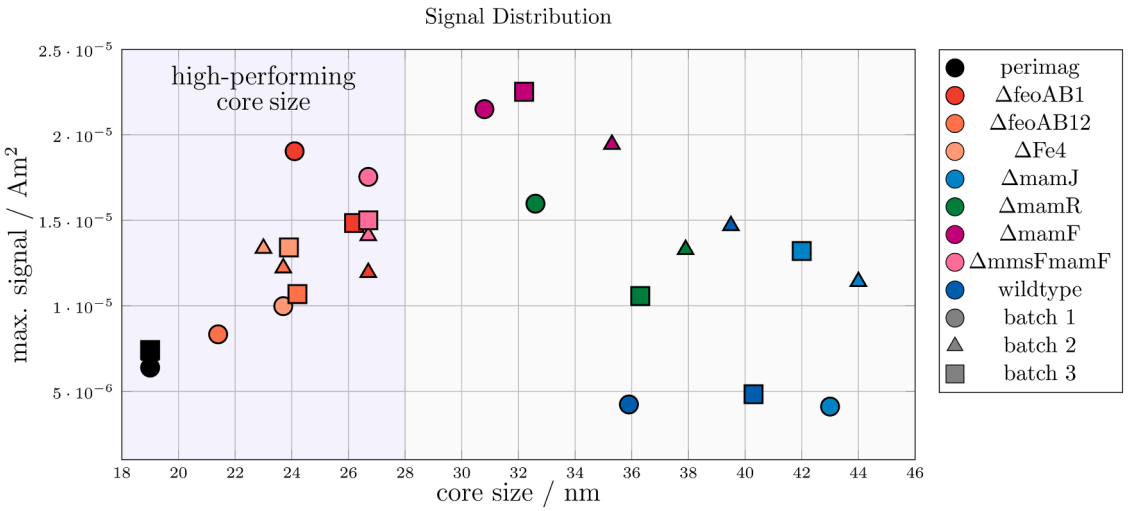

Fig. 4. Maximum MPS signal response distribution for three biological replicates of magnetosomes and *perimag*. For each replicate, the maximum magnetic moment in time domain is given in relation to the mean iron-oxide core size extracted from TEM images. All replicates of Δ*feoAB1,* Δ*feoAB12,* Δ*Fe4*, and Δ*mmsF/* Δ*mamF* provide core sizes between 20 nm and 28 nm. Among the high-performing candidates for multi-dimensional drive-field excitation, Δ*feoAB1* shows the largest magnetic moment.

candidate, Δ*feoAB1*, is shown in Fig. 5. On the left, the hysteresis curves at various drive-field amplitudes, commonly used in the MPI field, are depicted. As the drive-field amplitude increased, the hysteresis loops became broader, indicating pronounced relaxation effects. In the middle, the FWHM results for Δ*feoAB1* and *perimag* are shown. Across all drive-field amplitudes, Δ*feoAB1* exhibits approximately 2 mT lower FWHM compared to *perimag*, indicating a narrower spatial response. On the right, the results of an MPS dilution series with six different iron concentrations are displayed to demonstrate the stability and reproducibility of the magnetosomes. The amplitude of the third harmonic increased almost linearly with rising iron concentrations, confirming the robust and stable signal characteristics of Δ*feoAB1*, with a high coefficient of determination ($R^2 = 0.9935$).

3.3. MPI system matrix and image reconstruction

With Δ*feoAB1* identified as the best-performing candidate, the tracer dynamics under multi-dimensional drive-field excitation were investigated. *perimag* was again used as the reference tracer, along with WT magnetosomes in their as-isolated and non-modified state, as well as magnetosomes purified from the Δ*mamJ* mutant strain, which had previously demonstrated promising imaging performance in the work of *Makela et al.* [69].

In Fig. 6, the measured two-dimensional (2D) system matrices of Δ*feoAB1*, Δ*mamJ*, WT magnetosomes, and *perimag* are compared. The SNR profiles of the x-channel provide a quantitative comparison of the system matrices across all frequencies. Δ*feoAB1* exhibited the highest SNR over a broad frequency range, whereas the SNR values of Δ*mamJ* and WT magnetosomes only surpassed those of *perimag* at frequencies up to approximately 350 kHz. For selected frequencies, highlighted in red in Fig. 6, complex color-coded system matrix patterns for the x-channel are shown [70]. With increasing frequency, pronounced phase shifts between the magnetosome samples and *perimag* became evident. Additionally, each pattern includes the SNR value normalized to *perimag*. In these comparisons, Δ*feoAB1* consistently retained clear superiority, while the SNR values of the other magnetosome samples converged toward those of *perimag* as the frequency increased. Using these system matrices, image reconstruction was performed for Δ*feoAB1*, Δ*mamJ*, WT magnetosomes, and *perimag*. The translation from MPS to multidimensional Lissajous drive-field excitation may fail for magnetic nanoparticles with pronounced chain characteristics or strong anisotropy, as they cannot follow rapid magnetic changes in all dimensions. Fig. 7 shows reconstructed images of two-line phantoms oriented in the x- and y-directions. The purpose of this experiment was solely to demonstrate that reconstruction is feasible at high tracer concentrations, rather than to evaluate spatial resolution or other imaging performance metrics. Due to the high concentration, successful reconstruction was achieved for all magnetosome types. Based on the SNR analysis presented in Fig. 6, Δ*feoAB1* exhibited superior SNR, and this tracer was therefore selected for all subsequent experiments.

For a direct quantitative comparison between the most promising candidate Δ*feoAB1* and *perimag*, the reconstructed images of a v-shaped

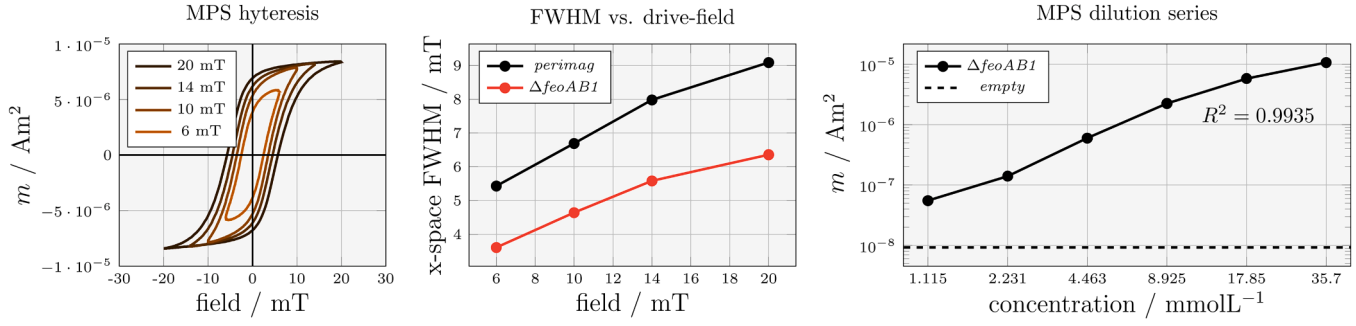

Fig. 5. MPS hysteresis loop, FWHM, and dilution series of Δ*feoAB1* magnetosomes. For several drive-field amplitudes commonly used in the MPI community, the hysteresis loops are shown. In the middle, the FWHM results obtained from static PSF measurements are presented. To verify signal linearity, the 3rd harmonic of the magnetic moment is plotted for six different iron concentrations, together with the value obtained from an empty measurement.

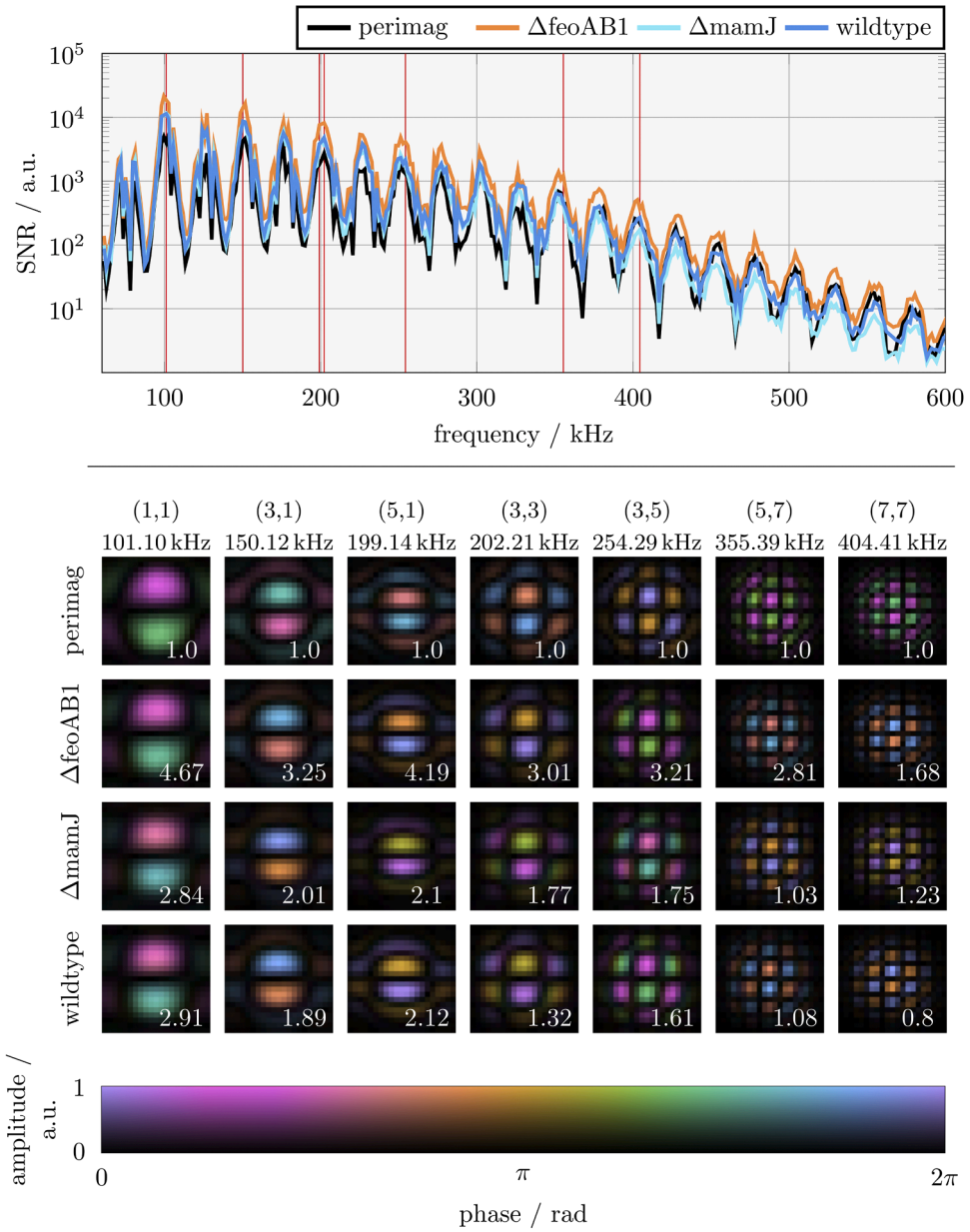

Fig. 6. MPI system matrix and SNR analysis. The SNR of the x-receive channel is shown for a 2D system matrix. For specific frequencies or mixing factors (k_x,k_y) marked in red, the according system matrix patterns are provided. The patterns are shown in a complex-coded color scheme, where the amplitude is encoded in the intensity and the phase is encoded in the color. For each frequency pattern, the SNR value normalized to *perimag* is noted in white.

phantom are presented in Fig. 8. Reconstruction quality was evaluated over consecutive frames ($n = 1000$) to ensure statistical robustness. The presented image obtained with Δ*feoAB1* displayed more distinct structural details of the phantom, with a more continuous and homogeneous signal profile. Both tracers exhibited reconstruction artifacts near the edges of the field of view (FOV).

Quantitative assessment was performed using a modeled mask, with the NRMSE and the SSIM calculated for each reconstructed frame and summarized as boxplots. The mean NRMSE was 0.157 for *perimag* and 0.112 for Δ*feoAB1*, indicating a substantially reduced reconstruction error for Δ*feoAB1*. Likewise, the mean SSIM increased from 0.828 for *perimag* to 0.912 for Δ*feoAB1*, demonstrating a clear improvement in structural fidelity and overall image quality. Statistical analysis confirmed significant differences between the tracers for both metrics ($p < 1 \times 10^{-16}$; Welch's *t*-test).

In Fig. 9, reconstruction results of a scaled anatomic rat model comprising the brain and liver phantoms are shown. All datasets were reconstructed using identical reconstruction parameters to ensure comparability. Due to minor robot misalignment between the two experiments, the phantoms corresponding to the different tracers exhibit slight relative spatial displacement. To ensure spatial correspondence, the reconstructed datasets were axially registered prior to visualization. For the displayed 2D reconstruction images, a reduced axial section of 31 pixels (instead of 40) was selected to improve structural visibility and comparability. Consistent with the visual impression, Δ*feoAB1* provides clearer structural representation in both organs compared to *perimag*. In the brain phantom, the areal structures corresponding to the three chambers are clearly resolved with Δ*feoAB1*, whereas they cannot be clearly distinguished in the *perimag* reconstruction. For quantitative assessment of background noise, the standard deviation (SD) of the signal was evaluated within the orange-marked region and normalized to the respective maximum reconstruction signal. In the brain phantom, the SD corresponds to 1.33% of the maximum signal for *perimag* and 0.43% for Δ*feoAB1*. In the liver phantom, the normalized SD values are

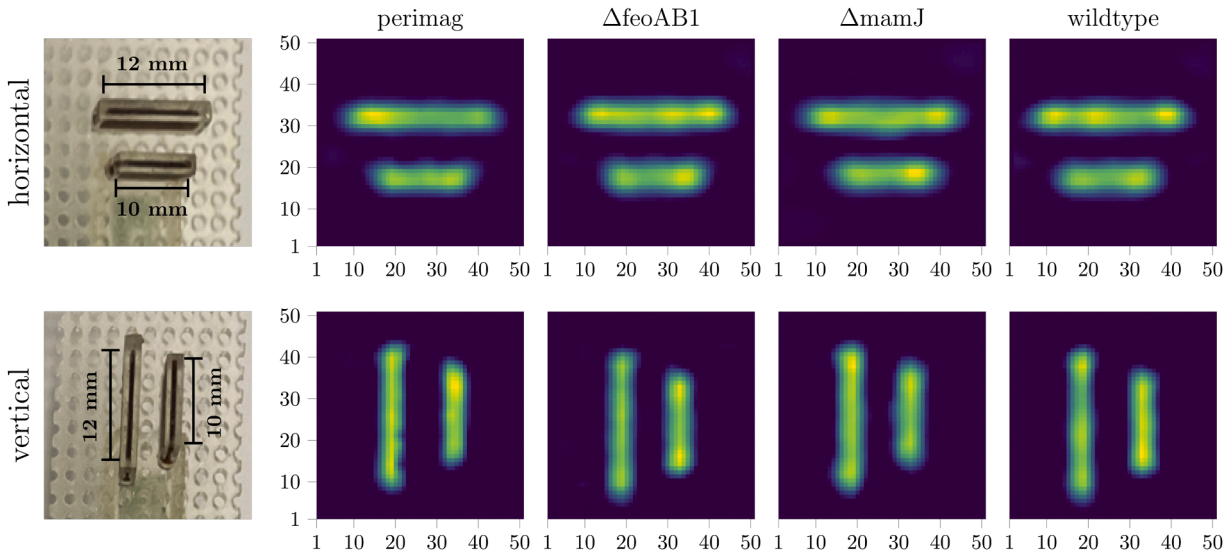

Fig. 7. MPI reconstruction of line-phantom. For both orientations in y-direction (horizontal) and in x-direction (vertical), the phantoms with an iron concentration of 35.7 mM can be resolved by all tracers.

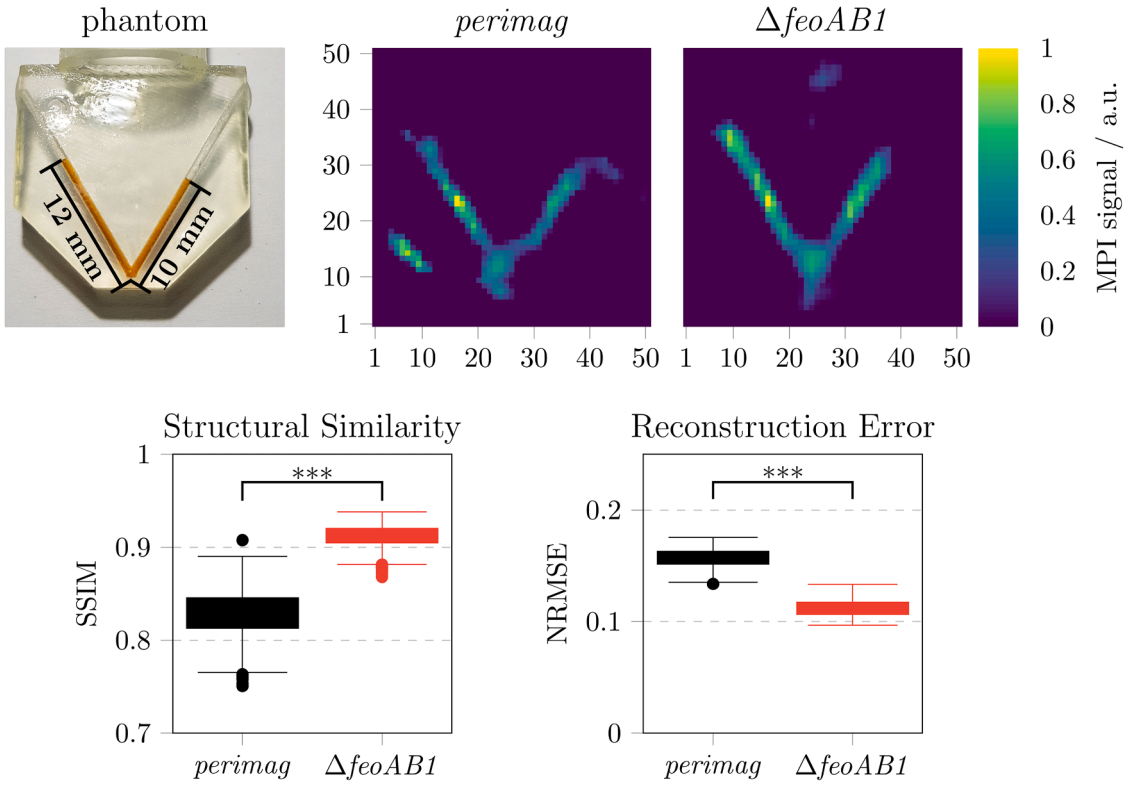

Fig. 8. MPI reconstruction of v-phantom (60° angular opening). A photograph of the v-shaped phantom and the corresponding MPI reconstructions obtained with *perimag* and *ΔfeoAB1* are presented. Quantitative evaluation of reconstruction accuracy over $n = 1000$ reconstructed frames is also shown, presented as boxplots of the structural similarity index measure (SSIM) and the normalized root mean squared error (NRMSE), calculated between each reconstructed frame and a modeled ground-truth mask. Higher SSIM and lower NRMSE values are observed for *ΔfeoAB1* magnetosomes, indicating improved image quality (*** $p < 1 \times 10^{-16}$; Welch's *t*-test).

0.056% for *perimag* and 0.026% for Δ*feoAB1*. The consistently lower relative background fluctuations observed for Δ*feoAB1* confirm its superior noise performance and enhanced image contrast under identical reconstruction conditions. For both MNPs and both organs, positioned relative to the rat phantom, corresponding surface renderings of the reconstructions are shown in Fig. S3.

3.4. Physicochemical characterization of ΔfeoAB1 magnetosomes

Our results identify Δ*feoAB1* as best-performing and probably most promising magnetosome type under the tested conditions. By applying our well-characterized purification scheme [51,52], particles with intact membranes were isolated. Thus, on TEM images a core-shell structure became visible that largely resembled WT magnetosomes, with the

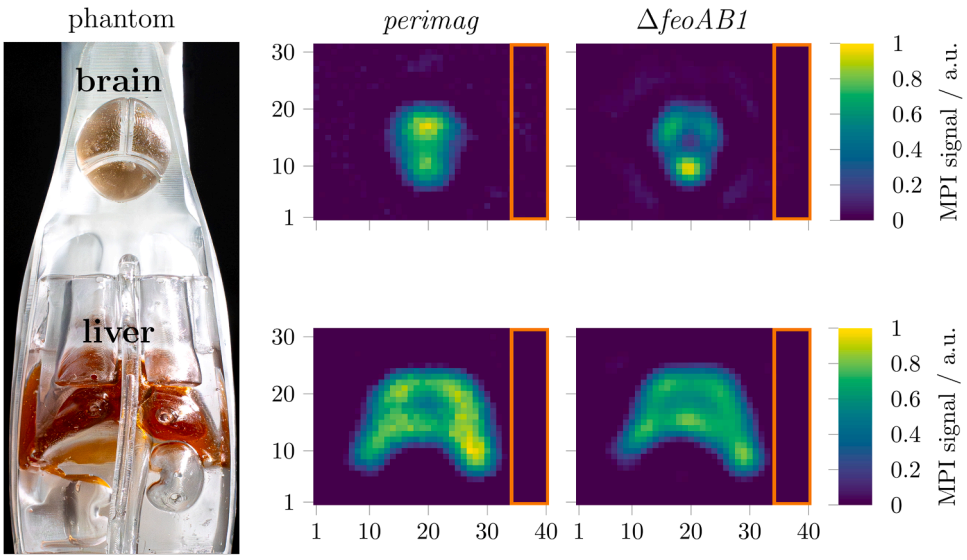

Fig. 9. MPI reconstruction of scaled rat phantom. The phantom was scaled 1.5× smaller than the original anatomical model, with organ-specific tracer concentrations applied to emulate a steady-state *in vivo* distribution (brain: 74 μg Fe mL^{-1}; liver: 270 μg Fe mL^{-1}). A photograph of the phantom showing both brain and liver sections is shown on the left. MPI reconstructions for the brain (top) and liver (bottom) are shown using *perimag* and *ΔfeoAB1* magnetosomes. Compared to *perimag, ΔfeoAB1* magnetosomes provide improved structural fidelity, with the three chambers of the brain clearly identifiable. For each reconstruction, the orange window marks the area where the standard deviation of the background signal was evaluated, showing lower background values for *ΔfeoAB1* and thus, improved image contrast.

magnetite cores being surrounded by an electron-light organic envelope representing the magnetosome membrane (Fig. S4-A). This is further supported by the particles' surface charge indicated by zeta potential values of −32.1 ± 4.8 mV (Δ*feoAB1*) and −34.7 ± 3.7 mV (WT) with no statistically significant difference between the two particle types (p = 0.11; Welch's *t*-test). For *perimag*, measured for comparison, the zeta potential was determined to be −9.5 ± 0.5 mV. All measurements were performed in ddH_2O at an iron concentration of 0.10 mg mL^{-1}, and obtained values suggest colloidal stability of the respective nanoparticle suspensions due to electrostatic repulsion.

These findings are also reflected in absorption-based sedimentation assays (Fig. S4-B), with WT and Δ*feoAB1* magnetosomes showing almost identical behavior. Accordingly, both particle suspensions remained highly stable throughout the 18 h observation period, with normalized sedimentation rates <2%. An initial albeit marginal sedimentation phase was observed during the first 5 h; however, absorption values declined by only ~1%. This was followed by an almost constant signal over the subsequent 13 h (<1% additional sedimentation). *perimag* exhibited similarly high colloidal stability, and only a negligible, near-linear absorption decrease was observed over the 18 h observation period (overall sedimentation rate <1%). Overall, the investigated magnetosome suspensions – and consequently Δ*feoAB1* – can be considered stable under the chosen experimental conditions, thereby providing a solid basis for further application-oriented studies.

4. Discussion

In the present study, we expand the spectrum of MPI tracers by introducing genetically engineered magnetosomes, biomineralized by magnetotactic bacteria, as highly promising candidates for next-generation MPI tracers. While previous studies such as *Kraupner et al.* [33] have already highlighted the potential of magnetosomes, our approach clearly differs from that of *Makela et al.* [69], who investigated whole living bacteria of the WT and the Δ*mamJ* mutant strain of *M. gryphiswaldense* as MPI tracers. Here, we systematically investigated an extended set of isolated and purified magnetosome types, derived from multiple genetically engineered bacterial deletion mutants. This allowed a detailed characterization of their morphology via TEM, their magnetic performance using MPS, and, ultimately, their imaging capability in MPI.

Despite some inherent polydispersity caused by the biological synthesis and maturation processes [52], several magnetosome variants fulfilled critical MPI requirements, including suitable core size and uniform cuboctahedral morphology [20,21]. Mutants such as Δ*mamR*, Δ*mamJ*, and Δ*mamF* produced magnetosomes with mean core sizes above 30 nm, exceeding the superparamagnetic size threshold and thus, exhibiting ferrimagnetic behavior [71]. In contrast, magnetosomes from Δ*feoAB1*, Δ*feoAB12*, Δ*Fe4*, and Δ*mmsF*/Δ*mamF* showed core sizes in the optimal range of 21–28 nm (as determined from TEM micrographs), classifying them as promising tracers. This size range closely matches the theoretically predicted optimal core size for MPI of approximately 28 nm [46]. Moreover, our results are consistent with the experimentally observed *relaxation wall*, indicating that further increases in the core size yield in undesired dominant magnetic relaxation effects [72].

Using MPS as a pre-screening tool, we defined two essential criteria to identify promising MPI tracers:

1. A magnetization signal response exceeding that of the commercial standard tracer *perimag*, and
2. The absence of strong relaxation effects, which indicate unfavorable particle size distributions, anisotropy, or agglomeration.

Magnetosomes of strain Δ*feoAB1* (~26 nm) emerged as the best-performing candidate, exhibiting a nearly 3-fold stronger MPS signal compared to *perimag* and showing no abnormal relaxation behavior. Biomedically, this 3-fold signal amplification is highly significant, as it fundamentally dictates the required contrast agent dose. A higher intrinsic signal allows for a substantial lowering of the injected iron concentration, effectively minimizing the systemic clearance burden on the reticuloendothelial system while maintaining exceptional spatial resolution.

The hysteresis analysis confirmed stable, non-aggregated particle behavior even at increasing drive-field amplitudes. The same trend was observed in the 1D evaluation of the PSF, where the FWHM for Δ*feoAB1* was consistently 2 mT lower than that of *perimag* across the investigated set of drive-field amplitudes. However, the 1D PSF FWHM does not fully

capture particle behavior under multidimensional Lissajous drive-field excitation; because relaxation effects introduce delays in the PSF, a tracer that appears favorable in 1D measurements may not faithfully follow the rapidly changing multidimensional fields, leading to degraded signal or contrast in practical Lissajous imaging. The dilution series of Δ*feoAB1* demonstrated a linear correlation between concentration and signal, indicating excellent stability and reproducibility. Importantly, these MPS findings translated directly to multidimensional MPI performance. Δ*feoAB1* showed the highest SNR values across a wide frequency range in 2D system matrices, outperforming both WT magnetosomes and Δ*mamJ* particles, which had been previously suggested as promising tracers [69]. While 2D imaging of line phantoms was feasible with all three magnetosome types, the quantitative comparison with *perimag* using the v-phantom clearly demonstrated the superior image quality and reconstruction accuracy achieved with Δ*feoAB1*. Even though improvements in quantitative measures such as NRMSE and SSIM were modest, they represent a significant step toward advancing MPI tracer technology. In particular, the approach reduced the influence of background artefacts and demonstrated consistently higher structural similarity with the reference mask across the full set of 1000 evaluated reconstructions. Reconstruction of the 3D-printed rat phantom shows that Δ*feoAB1* provides clearer structural delineation and lower background noise than *perimag*, with improved resolution of fine features such as the brain chambers. Using realistic phantoms allows direct comparison of tracer performance while minimizing animal use and suffering. In the absence of a defined *in vivo* application, these phantom experiments provide sufficient insight into MPI performance, guiding future *in vivo* studies after tracer optimization.

Our results also provide important context for studies using whole cells as MPI tracers. *Makela et al.* [69] observed increased MPI signals when using intact Δ*mamJ* cells *in vivo*, likely due to altered intracellular magnetosome clustering. However, in our experiments, intact WT and Δ*mamJ* cells showed only weak MPS responses compared to isolated magnetosomes (Table S3), highlighting the limitations of whole-cell approaches for MPI. Furthermore, the use of living bacteria poses substantial biosafety challenges, whereas purified magnetosomes, whose biocompatibility has been demonstrated in multiple studies [38,39,52,73–76], represent a far safer and more scalable solution.

So far, a couple of different studies have already comprehensively evaluated potential biological effects by critically assessing several biocompatibility parameters, including cell viability (*i.e.*, metabolic activity), cell death events during magnetosome treatment, and potential effects on cell proliferation. Data obtained from multiple assays were combined to provide an integrated overall assessment. Across the different cell lines tested (cancer lines as well as primary cells), only minor effects on viability were observed, even at increased magnetosome concentrations [38,39,52]. Accordingly, magnetosomes were considered biocompatible [77] even for concentrations exceeding those usually applied in *in vivo* settings. Furthermore, data available so far confirm high blood compatibility, and only slight but not significant complement activation was observed, with no indications for plasma coagulation or hemolysis [78].

Despite the presence of lipopolysaccharide (LPS) components originating from the cell wall of the bacterial production strain [78], in initial animal testings on rodents no pyrogenic effects were observed [73,76,79]. In addition, strategies for endotoxin camouflage and removal have been suggested [78] including coating with biocompatible polymers such as serum proteins [80,81] and the introduction of further purification steps of magnetosome suspensions, for instance the treatment with mild detergents such as Triton X-100 [82], ion-exchange chromatography, affinity adsorbents, gel filtration, or ultrafiltration [83].

Overall, our study establishes Δ*feoAB1* magnetosomes as highly optimized, genetically engineered MPI tracers. By tailoring the magnetosome biosynthesis through genetic engineering, we have demonstrated a precise and reproducible method to create nanoparticles with ideal MPI characteristics, overcoming key limitations of synthetic tracers. This work provides a strong foundation for future studies focused on *in vivo* imaging, surface functionalization for targeted applications, and the eventual translation of biologically produced tracers into clinical MPI, thereby significantly expanding the potential of this powerful imaging modality.

5. Conclusion and outlook

In conclusion, our comprehensive evaluation of genetically engineered magnetosomes using TEM, MPS, and MPI identified Δ*feoAB1* magnetosomes as a highly promising candidate for next-generation MPI tracers. By utilizing genetic engineering to bypass the structural limitations of conventional chemical synthesis, this study provides a clear translational pathway for using highly uniform biogenic magnetosomes as predictable, reproducible, high-contrast diagnostics in preclinical and future clinical MPI applications. These particles exhibited an optimal core-size distribution, resulting in a strong and stable MPS signal as well as superior image quality in MPI reconstructions compared to the established synthetic tracer *perimag*. The genetically encoded biosynthesis of magnetosomes provides a unique advantage by allowing precise and reproducible tuning of particle properties through targeted genetic modifications, thereby overcoming key limitations of chemically synthesized nanoparticles.

Currently, the magnetite cores of the investigated magnetosomes are surrounded only by their natural biological membrane. While this native coating offers some inherent stabilization, it may also promote particle–particle interactions, potentially affecting colloidal stability and MPI performance. Future *in vitro* surface functionalization, such as the addition of dextran or resin shells [84,85], could further improve stability, biocompatibility, and performance, especially when the particles are suspended in physiological buffers such as PBS.

Looking ahead, Δ*feoAB1* magnetosomes hold significant potential for *in vivo* MPI applications, including real-time vascular imaging, perfusion studies, and cell tracking. Their genetic tunability opens new opportunities for developing tracers with tailored magnetic properties [31,32] or functionalized surfaces for targeted imaging [34,86–88]. Moreover, their biological origin and reproducible biosynthesis address a critical bottleneck in MPI translation by providing a scalable and consistent source of high-performance tracers. Future work should focus on *in vivo* validation, regulatory assessment, and the development of clinically compatible production and stabilization processes.

Furthermore, as magnetosomes were already successfully tested as potential agents for magnetic fluid hyperthermia (MFH) [30,89,90], their application range might be extended toward a platform that efficiently combines diagnostic and therapeutic modalities. In fact, Δ*feoAB1* magnetosomes have already been investigated for dual functionality as MPI tracers and MFH heat mediators, providing substantially higher imaging SNR and MFH temperature compared to synthetic MNP formulations, thereby highlighting their theranostic potential [91].

By establishing genetically engineered magnetosomes as powerful MPI tracers, this study paves the way for advancing MPI from a preclinical research tool toward a clinically relevant imaging modality, with broad applications across biomedicine. Ultimately, such tracers could play a transformative role in modern medical imaging, enabling highly sensitive, safe, and real-time diagnostics.

CRediT authorship contribution statement

Florian Thieben: Writing – review & editing, Writing – original draft, Validation, Methodology, Investigation, Formal analysis, Data curation. **Frank Mickoleit:** Writing – review & editing, Writing – original draft, Supervision, Project administration, Methodology, Investigation, Data curation. **René Uebe:** Writing – review & editing, Formal analysis, Data curation. **Sophia Tessaro:** Investigation, Formal analysis. **Marina V. Dziuba:** Methodology, Investigation, Formal analysis. **Javier Rández-Garbayo:** Writing – original draft, Investigation, Formal

analysis. **Tim Magnus:** Writing – review & editing, Funding acquisition. **Mandy Ahlborg:** Writing – review & editing, Methodology, Investigation. **Justin Ackers:** Writing – review & editing, Methodology, Investigation. **Peter Ludewig:** Writing – review & editing, Validation, Investigation, Funding acquisition, Formal analysis, Data curation, Conceptualization. **Dirk Schüler:** Writing – review & editing, Validation, Supervision, Resources, Funding acquisition, Conceptualization. **Tobias Knopp:** Writing – review & editing, Supervision, Resources, Project administration, Funding acquisition, Conceptualization.

Declaration of competing interest

The authors declare that they have no known competing financial interests or personal relationships that could have appeared to influence the work reported in this paper.

Acknowledgements

The authors thank Matthias Schlotter for technical assistance with cultivation of *M. gryphiswaldense* strains and magnetosome isolation, and Jakob J. Beierl for support in DLS measurements (both Dept. Microbiology, University of Bayreuth). This work was funded in part by the European Research Council (ERC-2023-PoC, grant "BacToMagicle" to D.S.) and the Federal Ministry of Education and Research (BMBF; grant MagBioFab to R.U. and D.S., grant MAGnetISE to P.L. and T.K.). Further funding was received from the Deutsche Forschungsgemeinschaft (DFG, German Research Foundation, INST 91/374-1 LAGG to R.U. and D.S., SCHU 1080/26-1 to D.S., LU 1924/1-2 to P.L., KN 1108/7-1 and KN 1108/2-2 to T.K.), and from the Fielmann Förderstiftung (to P.L. and T.M.).

Supplementary materials

Supplementary material associated with this article can be found, in the online version, at doi:10.1016/j.actbio.2026.05.048.

References

[1] B. Gleich, J. Weizenecker, Tomographic imaging using the nonlinear response of magnetic particles, Nature 435 (2005) 1214–1217.
[2] M. Graeser, P. Ludewig, P. Szwargulski, F. Foerger, T. Liebing, N.D. Forkert, F. Thieben, T. Magnus, T. Knopp, Design of a head coil for high resolution mouse brain perfusion imaging using magnetic particle imaging, Phys. Med. Biol. 65 (2020) 235007.
[3] O. Kosch, U. Heinen, L. Trahms, F. Wiekhorst, Preparing system functions for quantitative MPI, Int. J. Magn. Part. Imaging 3 (2017) 1706002.
[4] F. Griese, T. Knopp, C. Gruettner, F. Thieben, K. Müller, S. Loges, P. Ludewig, N. Gdaniec, Simultaneous magnetic particle imaging and navigation of large superparamagnetic nanoparticles in bifurcation flow experiments, J. Magn. Magn. Mater. 498 (2020) 166206.
[5] M. Möddel, F. Griese, T. Kluth, T. Knopp, Estimating orientation using multi-contrast MPI, Int. J. Magn. Part. Imaging 6 (2020) 2009023.
[6] O. Buchholz, K. Sajjamark, J. Franke, H. Wie, A. Behrends, C. Münkel, C. Grüttner, P. Levan, D. von Elverfeldt, M. Graeser, T. Buzug, S. Bär, U.G. Hofmann, *In situ* theranostic platform combining highly localized magnetic fluid hyperthermia, magnetic particle imaging, and thermometry in 3D, Theranostics 14 (2024) 324–340.
[7] P. Szwargulski, M. Wilmes, E. Javidi, F. Thieben, M. Graeser, M. Koch, C. Gruettner, G. Adam, C. Gerloff, T. Magnus, T. Knopp, P. Ludewig, Monitoring intracranial cerebral hemorrhage using multicontrast real-time magnetic particle imaging, ACS Nano 14 (2020) 13913–13923.
[8] P. Ludewig, N. Gdaniec, J. Sedlacik, N.D. Forkert, P. Szwargulski, M. Graeser, G. Adam, M.G. Kaul, K.M. Krishnan, R.M. Ferguson, A.P. Khandhar, P. Walczak, J. Fiehler, G. Thomalla, C. Gerloff, T. Knopp, T. Magnus, Magnetic particle imaging for real-time perfusion imaging in acute stroke, ACS Nano 11 (2017) 10480–10488.
[9] X.Y. Zhou, Z.W. Tay, P. Chandrasekharan, E.Y. Yu, D.W. Hensley, R. Orendorff, K. E. Jeffris, D. Mai, B. Zheng, P.W. Goodwill, S.M. Conolly, Magnetic particle imaging for radiation-free, sensitive and high-contrast vascular imaging and cell tracking, Curr. Opin. Chem. Biol. 45 (2018) 131–138.
[10] P. Ludewig, M. Graeser, N.D. Forkert, F. Thieben, J. Rández-Garbayo, J. Rieckhoff, K. Lessmann, F. Förger, P. Szwargulski, T. Magnus, T. Knopp, Magnetic particle imaging for assessment of cerebral perfusion and ischemia, WIREs Nanomed. Nanobiotechnol. 14 (2022) e1757.
[11] P. Vogel, M.A. Rückert, C. Greiner, J. Günther, T. Reichl, T. Kampf, T.A. Bley, V. C. Behr, S. Herz, iMPI: portable human-sized magnetic particle imaging scanner for real-time endovascular interventions, Sci. Rep. 13 (2023) 10472.
[12] E. Mattingly, M. Śliwiak, E. Mason, J. Chacon-Caldera, A. Barksdale, F.H. Niebel, K. Herb, M. Graeser, L.L. Wald, Design, construction and validation of a magnetic particle imaging (MPI) system for human brain imaging, Phys. Med. Biol. 70 (2025) 015019.
[13] F. Thieben, F. Foerger, F. Mohn, N. Hackelberg, M. Boberg, J.P. Scheel, M. Möddel, M. Graeser, T. Knopp, System characterization of a human-sized 3D real-time magnetic particle imaging scanner for cerebral applications, Commun. Eng. 3 (2024) 47.
[14] F. Mohn, K. Scheffler, J. Ackers, A. Weimer, F. Wegner, F. Thieben, M. Ahlborg, P. Vogel, M. Graeser, T. Knopp, Characterization of the clinically approved MRI tracer resotran for magnetic particle imaging in a comparison study, Phys. Med. Biol. 69 (2024) 135014.
[15] S. Biederer, T. Knopp, T.F. Sattel, K. Lüdtke-Buzug, B. Gleich, J. Weizenecker, J. Borgert, T.M. Buzug, Magnetization response spectroscopy of superparamagnetic nanoparticles for magnetic particle imaging, J. Phys. D Appl. Phys. 42 (2009) 205007.
[16] R.M. Ferguson, K.R. Minard, K.M. Krishnan, Optimization of nanoparticle core size for magnetic particle imaging, J. Magn. Magn. Mater. 321 (2009) 1548–1551.
[17] A.S. Teja, P.Y. Koh, Synthesis, properties, and applications of magnetic iron oxide nanoparticles, Prog. Cryst. Growth Charact. Mater. 55 (2009) 22–45.
[18] J. Mosayebi, M. Kiyasatfar, S. Laurent, Synthesis, functionalization, and sesign of magnetic nanoparticles for theranostic applications, Adv. Healthc. Mater. 6 (2017) 1700306.
[19] K. Turcheniuk, A.V. Tarasevych, V.P. Kukhar, R. Boukherroub, S. Szunerits, Recent advances in surface chemistry strategies for the fabrication of functional iron oxide based magnetic nanoparticles, Nanoscale 5 (2013) 10729–10752.
[20] L.M. Bauer, S.F. Situ, M.A. Griswold, A.C.S. Samia, Magnetic particle imaging tracers: state-of-the-art and future directions, J. Phys. Chem. Lett. 6 (2015) 2509–2517.
[21] A. Tomitaka, R.M. Ferguson, A.P. Khandhar, S.J. Kemp, S. Ota, K. Nakamura, Y. Takemura, K.M. Krishnan, Variation of magnetic particle imaging tracer performance with amplitude and frequency of the applied magnetic field, IEEE Trans. Magn. 51 (2015) 1–4.
[22] M.M. Saari, M.H. Sulaiman, N.A.C. Lah, Z. Aziz, K. Sakai, T. Kiwa, K. Tsukada, Properties of single- and multi-core magnetic nanoparticles assessed by magnetic susceptibility measurements, J. Magn. Magn. Mater. 528 (2021) 167812.
[23] A.A. Ozaslan, M. Utkur, U. Canpolat, M.A. Tuncer, K.K. Oguz, E.U. Saritas, PNS limits for human head-size MPI systems: preliminary results, Int. J. Magn. Part. Imaging 8 (2022) 2203028.
[24] A.C. Barksdale, N.G. Ferris, E. Mattingly, M. Śliwiak, B. Guerin, L.L. Wald, M. Davids, V. Klein, Measurement of peripheral nerve magnetostimulation thresholds of a head solenoid coil between 200 Hz and 88.1 kHz, IEEE J. Transl. Eng. Health Med. 13 (2025) 275–285.
[25] R. Uebe, D. Schüler, Magnetosome biogenesis in magnetotactic bacteria, Nat. Rev. Microbiol. 14 (2016) 621–637.
[26] D. Schüler, F.D. Müller, Biosynthesis and intracellular organization of magnetosomes in magnetotactic bacteria, in: D. Jendrossek (Ed.), Bacterial Organelles and Organelle-Like Inclusions, Microbiology Monographs 34, Springer, Cham, 2020, pp. 53–70.
[27] D. Schüler, M. Dziuba, D. Pfeiffer, R. Uebe, Biosynthesis and function of magnetic organelles in magnetotactic bacteria, Nat. Rev. Microbiol. 24 (2026) 168–182.
[28] A. Fischer, M. Schmitz, B. Aichmayer, P. Fratzl, D. Faivre, Structural purity of magnetite nanoparticles in magnetotactic bacteria, J. R. Soc. Interface 8 (2011) 1011–1018.
[29] A. Lohße, S. Borg, O. Raschdorf, I. Kolinko, É. Tompa, M. Pósfai, D. Faivre, J. Baumgartner, D. Schüler, Genetic dissection of the *mamAB* and *mms6* operons reveals a gene set essential for magnetosome biogenesis in *Magnetospirillum gryphiswaldense*, J. Bacteriol. 196 (2014) 2658–2669.
[30] R. Hergt, R. Hiergeist, M. Zeisberger, D. Schüler, U. Heyen, I. Hilger, W.A. Kaiser, Magnetic properties of bacterial magnetosomes as potential diagnostic and therapeutic tools, J. Magn. Magn. Mater. 293 (2005) 80–86.
[31] M. Kumari, M. Widdrat, É. Tompa, R. Uebe, D. Schüler, M. Pósfai, D. Faivre, A. M. Hirt, Distinguishing magnetic particle size of iron oxide nanoparticles with first-order reversal curves, J. Appl. Phys. 116 (2014) 124304.
[32] R. Taukulis, M. Widdrat, M. Kumari, D. Heinke, M. Rumpler, É. Tompa, R. Uebe, A. Kraupner, A. Cēbers, D. Schüler, M. Pósfai, A.M. Hirt, D. Faivre, Magnetic iron oxide nanoparticles as MRI contrast agents – a comprehensive physical and theoretical study, Magnetohydrodynamics 51 (2015) 721–747.
[33] A. Kraupner, D. Eberbeck, D. Heinke, R. Uebe, D. Schüler, A. Briel, Bacterial magnetosomes – nature's powerful contribution to MPI tracer research, Nanoscale 9 (2017) 5788–5793.
[34] S. Schuerle, M. Furubayashi, A.P. Soleimany, T. Gwisai, W. Huang, C. Voigt, S. N. Bhatia, Genetic encoding of targeted magnetic resonance imaging contrast agents for tumor imaging, ACS Synth. Biol. 9 (2020) 392–401.
[35] J. Xu, J. Hu, L. Liu, L. Li, X. Wang, H. Zhang, W. Jiang, J. Tian, Y. Li, J. Li, Surface expression of protein A on magnetosomes and capture of pathogenic bacteria by magnetosome/antibody complexes, Front. Microbiol. 5 (2014) 136.
[36] F. Mickoleit, C.B. Borkner, M. Toro-Nahuelpan, H.M. Herold, D.S. Maier, J. M. Plitzko, T. Scheibel, D. Schüler, *In vivo* coating of bacterial magnetic nanoparticles by magnetosome expression of spider silk-inspired peptides, Biomacromolecules 19 (2018) 962–972.
[37] F. Mickoleit, S. Rosenfeldt, M. Toro-Nahuelpan, M. Schaffer, A.S. Schenk, J. M. Plitzko, D. Schüler, High-yield production, characterization, and

functionalization of recombinant magnetosomes in the synthetic bacterium *Rhodospirillum rubrum 'magneticum'*, Adv. Biol. 5 (2021) 2101017.
[38] F. Mickoleit, C. Jörke, R. Richter, S. Rosenfeldt, S. Markert, I. Rehberg, A.S. Schenk, O. Bäumchen, D. Schüler, J.H. Clement, Long-term stability, biocompatibility, and magnetization of suspensions of isolated bacterial magnetosomes, Small 19 (2023) 2206244.
[39] F. Mickoleit, C. Jörke, S. Geimer, D.S. Maier, J.P. Müller, J. Demut, C. Gräfe, D. Schüler, J.H. Clement, Biocompatibility, uptake and subcellular localization of bacterial magnetosomes in mammalian cells, Nanoscale Adv. 3 (2021) 3799–3815.
[40] B.M. Moskowitz, R.B. Frankel, P.J. Flanders, R.P. Blakemore, B.B. Schwartz, Magnetic properties of magnetotactic bacteria, J. Magn. Magn. Mater. 73 (1988) 273–288.
[41] J.L. Kirschvink, Magnetite biomineralization and geomagnetic sensitivity in higher animals: an update and recommendations for future study, Bioelectromagnetics 10 (1989) 239–259.
[42] R.Y. Tsien, Imagining imaging's future, Proc. Natl. Acad. Sci. USA 87 (1990) 3112–3116.
[43] A. Lohße, S. Ullrich, E. Katzmann, S. Borg, G. Wanner, M. Richter, B. Voigt, T. Schweder, D. Schüler, Functional analysis of the magnetosome island in *Magnetospirillum gryphiswaldense*: the *mamAB* operon is sufficient for magnetite biomineralization, PLoS ONE 6 (2011) e25561.
[44] D. Heinke, A. Kraupner, D. Eberbeck, D. Schmidt, P. Radon, R. Uebe, D. Schüler, A. Briel, MPS and MRI efficacy of magnetosomes from wild-type and mutant bacterial strains, Int. J. Magn. Part. Imaging 3 (2017) 1706004.
[45] F. Mickoleit, F. Thieben, S. Tessaro, P. Ludewig, D. Schüler, J. Rández-Garbayo, R. Uebe, T. Knopp, Development of optimized magnetic particle imaging tracers utilizing genetically engineered magnetosomes, Int. J. Magn. Part. Imaging 9 (2023) 2303066.
[46] C. Shasha, E. Teeman, K.M. Krishnan, Nanoparticle core size optimization for magnetic particle imaging, Biomed. Phys. Eng. Express 5 (2019) 055010.
[47] A. Scheffel, M. Gruska, D. Faivre, A. Linaroudis, J.M. Plitzko, D. Schüler, An acidic protein aligns magnetosomes along a filamentous structure in magnetotactic bacteria, Nature 440 (2006) 110–114.
[48] U. Heyen, D. Schüler, Growth and magnetosome formation by microaerophilic Magnetospirillum strains in an oxygen-controlled fermentor, Appl. Microbiol. Biotechnol. 61 (2003) 536–544.
[49] C. Lang, D. Schüler, Expression of green fluorescent protein fused to magnetosome proteins in microaerophilic magnetotactic bacteria, Appl. Environ. Microbiol. 74 (2008) 4944–4953.
[50] S. Tessaro, M. Schüritz, V. Jérôme, R. Freitag, R. Uebe, Controlled low-oxygen supply uncouples magnetite nucleation and crystal growth in *Magnetospirillum gryphiswaldense*, Microb. Biotechnol. 19 (2026) e70349.
[51] O. Raschdorf, D. Schüler, R. Uebe, Preparation of bacterial magnetosomes for proteome analysis. Microbial Proteomics: Methods and Protocols, Springer New York, New York, NY, 2018, pp. 45–57.
[52] S. Rosenfeldt, F. Mickoleit, C. Jörke, J.H. Clement, S. Markert, V. Jérôme, S. Schwarzinger, R. Freitag, D. Schüler, R. Uebe, A.S. Schenk, Towards standardized purification of bacterial magnetic nanoparticles for future *in vivo* applications, Acta Biomater. 120 (2021) 293–303.
[53] F. Mickoleit, V. Jérôme, R. Freitag, D. Schüler, Bacterial magnetosomes as novel platform for the presentation of immunostimulatory, membrane-bound ligands in cellular biotechnology, Adv. Biosyst. 4 (2020) 1900231.
[54] T.J. Collins, ImageJ for microscopy, Biotechniques 43 (2007) 25–30.
[55] D. Eberbeck, C.L. Dennis, N.F. Huls, K.L. Krycka, C. Gruttner, F. Westphal, Multicore magnetic nanoparticles for magnetic particle imaging, IEEE Trans. Magn. 49 (2012) 269–274.
[56] K. Pansegrau, P. Radon, A. Jaufenthaler, F. Wiekhorst, D. Baumgarten, Comparison of magnetic nanoparticle immobilization methods using MPS and MRX, Nanoscale 18 (2026) 9756–9773, https://doi.org/10.1039/d5nr05283a.
[57] F. Thieben, T. Knopp, M. Boberg, F. Foerger, M. Graeser, M. Möddel, On the receive path calibration of magnetic particle imaging systems, IEEE Trans. Instrum. Meas. 72 (2022) 1–15.
[58] E. Aderhold, J. Ackers, P. Stagge, J.P. Scheel, F. Wegner, M.J. Buhné, T. Buzug, M. Ahlborg, M. Graeser, Development and assessment of a 1D-MPS, Int. J. Magn. Part. Imaging 11 (2025) 2503056.
[59] L.R. Croft, P.W. Goodwill, S.M. Conolly, Relaxation in x-space magnetic particle imaging, IEEE Trans. Med. Imaging 31 (2012) 2335–2342.
[60] M.T. Arslan, A.A. Özaslan, S. Kurt, Y. Muslu, E.U. Saritas, Rapid TAURUS for relaxation-based color magnetic particle imaging, IEEE Trans. Med. Imaging 41 (2022) 3774–3786.
[61] J. Rahmer, J. Weizenecker, B. Gleich, J. Borgert, Analysis of a 3-D system function measured for magnetic particle imaging, IEEE Trans. Med. Imaging 31 (2012) 1289–1299.
[62] J. Franke, U. Heinen, H. Lehr, A. Weber, F. Jaspard, W. Ruhm, M. Heidenreich, V. Schulz, System characterization of a highly integrated preclinical hybrid MPI-MRI scanner, IEEE Trans. Med. Imaging 35 (2016) 1993–2004.
[63] T. Knopp, P. Szwargulski, F. Griese, M. Grosser, M. Boberg, M. Möddel, MPIReco.jl: Julia package for image reconstruction in MPI, Int. J. Magn. Part. Imaging 5 (2019) 1907001.
[64] K. Scheffler, M. Boberg, T. Knopp, Solving the MPI reconstruction problem with automatically tuned regularization parameters, Phys. Med. Biol. 69 (2024) 045024.
[65] M. Exner, P. Szwargulski, T. Knopp, M. Graeser, P. Ludewig, 3D printed anatomical model of a rat for medical imaging, Curr. Dir. Biomed. Eng. 5 (2019) 187–190.
[66] A. Möglich, An open-source, cross-platform resource for nonlinear least-squares curve fitting, J. Chem. Educ. 95 (2018) 2273–2278.
[67] K. Grünberg, C. Wawer, B.M. Tebo, D. Schüler, A large gene cluster encoding several magnetosome proteins is conserved in different species of magnetotactic bacteria, Appl. Environ. Microbiol. 67 (2001) 4573–4582.
[68] A.P. Philipse, D. Maas, Magnetic colloids from magnetotactic bacteria: chain formation and colloidal stability, Langmuir 18 (2002) 9977–9984.
[69] A.V. Makela, M.A. Schott, C.S. Madsen, E.M. Greeson, C.H. Contag, Magnetic particle imaging of magnetotactic bacteria as living contrast agents is improved by altering magnetosome arrangement, Nano Lett. 22 (2022) 4630–4639.
[70] H. Albers, T. Knopp, M. Möddel, M. Boberg, T. Kluth, Modeling the magnetization dynamics for large ensembles of immobilized magnetic nanoparticles in multi-dimensional magnetic particle imaging, J. Magn. Magn. Mater. 543 (2022) 168534.
[71] A.R. Muxworthy, W. Williams, Critical superparamagnetic/single-domain grain sizes in interacting magnetite particles: implications for magnetosome crystals, J. R. Soc. Interface 6 (2009) 1207–1212.
[72] Z.W. Tay, D.W. Hensley, E.C. Vreeland, B. Zheng, S.M. Conolly, The relaxation wall: experimental limits to improving MPI spatial resolution by increasing nanoparticle core size, Biomed. Phys. Eng. Express 3 (2017) 035003.
[73] X. Nan, Y. Teng, J. Tian, Z. Hu, Q. Fang, A comprehensive assessment of the biocompatibility of *Magnetospirillum gryphiswaldense* MSR-1 bacterial magnetosomes *in vitro* and *in vivo*, Toxicology 462 (2021) 152949.
[74] X. Nan, W. Lai, D. Li, J. Tian, Z. Hu, Q. Fang, Biocompatibility of bacterial magnetosomes as MRI contrast agent: a long-term *in vivo* follow-up study, Nanomaterials 11 (2021) 1235.
[75] M. Haripriyaa, K. Suthindhiran, Investigation of pharmacokinetics and immunogenicity of magnetosomes, Artif. Cells Nanomed. Biotechnol. 52 (2024) 69–83.
[76] T. Revathy, M.A. Jayasri, K. Suthindhiran, Toxicity assessment of magnetosomes in different models, 3 Biotech 7 (2017) 126.
[77] DIN Deutsches Institut für Normen e.V. Biologische Beurteilung von Medizinprodukten - Teil 5: Prüfungen auf *in-vitro*-Zytotoxizität (ISO 10993-5: 2009); Deutsche Fassung EN ISO 10993-5:2009. 2009.
[78] F. Mickoleit, F. Pfister, B. Friedrich, S. Markert, A. Kerpes, C. Janko, S. Lyer, C. Alexiou, D. Schüler, R. Tietze, Assessing cytotoxicity, endotoxicity, and blood compatibility of nanoscale iron oxide magnetosomes for biomedical applications, ACS Appl. Nano Mater. 7 (2024) 1278–1288.
[79] J. Sun, T. Tang, J. Duan, P.X. Xu, Z. Wang, Y. Zhang, L. Wu, Y. Li, Biocompatibility of bacterial magnetosomes: acute toxicity, immunotoxicity and cytotoxicity, Nanotoxicology 4 (2010) 271–283.
[80] W. Lai, D. Li, Q. Wang, X. Nan, Z. Xiang, Y. Ma, Y. Liu, J. Chen, J. Tian, Q.A. Fang, Protein corona adsorbed to a bacterial magnetosome affects its cellular uptake, Int. J. Nanomed. 15 (2020) 1481–1498.
[81] J. Schwan, S. Markert, S. Rosenfeldt, D. Schüler, F. Mickoleit, A.S. Schenk, Comparing the colloidal stabilities of commercial and biogenic iron oxide nanoparticles that have potential *in vitro/in vivo* applications, Molecules 28 (2023) 4895.
[82] L. Kondratova, O. Kondratov, R. Ragheb, S. Zolotukhin, Removal of endotoxin from rAAV samples using a simple detergent-based protocol, Mol. Ther. Methods Clin. Dev. 15 (2019) 112–119.
[83] P.O. Magalhães, A.M. Lopes, P.G. Mazzola, C. Rangel-Yagui, T.C. Penna, A. Pessoa Jr., Methods of endotoxin removal from biological preparations: a review, J. Pharm. Pharm. Sci. 10 (2007) 388–404.
[84] J.H. Clement, M. Schwalbe, N. Buske, K. Wagner, M. Schnabelrauch, P. Görnert, K. O. Kliche, K. Pachmann, W. Weitschies, K. Höffken, Differential interaction of magnetic nanoparticles with tumor cells and peripheral blood cells, J. Cancer Res. Clin. Oncol. 132 (2006) 287–292.
[85] J. Feye, J. Matthias, A. Fischer, D. Rudolph, J. Treptow, R. Popescu, J. Franke, A. L. Exarhos, Z.A. Boekelheide, D. Gerthsen, C. Feldmann, P.W. Roesky, E.S. Rösch, SMART RHESINs – superparamagnetic magnetite architecture made of phenolic resin hollow spheres coated with Eu(III) containing silica nanoparticles for future quantitative magnetic particle imaging applications, Small 19 (2023) 2301997.
[86] M. Boucher, F. Geffroy, S. Prévéral, L. Bellanger, E. Selingue, G. Adryanczyk-Perrier, M. Péan, C.T. Lefèvre, D. Pignol, N. Ginet, S. Mériaux, Genetically tailored magnetosomes used as MRI probe for molecular imaging of brain tumor, Biomaterials 121 (2017) 167–178.
[87] M. Hafsi, S. Preveral, C. Hoog, J. Hérault, G.A. Perrier, C.T. Lefèvre, H. Michel, D. Pignol, J. Doyen, T. Pourcher, O. Humbert, J. Thariat, B. Cambien, RGD-functionalized magnetosomes are efficient tumor radioenhancers for X-rays and protons, Nanomedicine 23 (2020) 102084.
[88] F. Mickoleit, J.J. Beierl, S. Markert, M.A. Klein, S.Y. Stäbler, D.S. Maier, D. Schüler, A versatile magnetic nanoplatform for plug-and-play functionalization: genetically programmable cargo loading to bacterial magnetosomes by SpyCatcher "click biology", ACS Nano 18 (2014) 27974–27987.
[89] R. Le Fèvre, M. Durand-Dubief, I. Chebbi, C. Mandawala, F. Lagroix, J.P. Valet, A. Idbaih, C. Adam, J.Y. Delattre, C. Schmitt, C. Maake, F. Guyot, E. Alphandéry, Enhanced antitumor efficacy of biocompatible magnetosomes for the magnetic hyperthermia treatment of glioblastoma, Theranostics 7 (2017) 4618–4631.
[90] T.N. Nguyen, I. Chebbi, R. Le Fèvre, F. Guyot, E. Alphandéry, Non-pyrogenic highly pure magnetosomes for efficient hyperthermia treatment of prostate cancer, Appl. Microbiol. Biotechnol. 107 (2023) 1159–1176.
[91] O. Buchholz, M. Dziuba, S. Markert, D. Schüler, U.G. Hofmann, S. Ilbey, J. Franke, F. Mickoleit, Magnetosomes: the future of theranostics? Int. J. Magn. Part. Imaging 12 (1) (2026) 2603022. Suppl 1.